Electronic stopping power and electronic energy-loss mechanism for a low-energy ion in TiN under channeling conditions

Yan-Long Fu [1,2] Zhong-Zheng Tang,[1,2] Wei Cheng,[1,2] Jia-Yong Zhong,[3] and Feng-Shou Zhang [1,2,4,*]

[1]*Key Laboratory of Beam Technology of the Ministry of Education, College of Nuclear Science and Technology, Beijing Normal University, Beijing 100875, China*
[2]*Institute of Radiation Technology, Beijing Academy of Science and Technology, Beijing 100875, China*
[3]*Astronomy Department, Beijing Normal University, Beijing 100875, China*
[4]*Center of Theoretical Nuclear Physics, National Laboratory of Heavy Ion Accelerator of Lanzhou, Lanzhou 730000, China*

The electronic stopping power of a low-energy proton in a crystalline TiN film is investigated by computer simulation based on the time-dependent density-functional theory. The calculated results show that the electronic stopping power of the small impact parameter coincides with the experimental data. By evaluating the channeling electronic density and the stopping force in different channels, the direction dependence of the electronic stopping power is explored and revealed. Along the $\langle 110 \rangle$ channel, the electronic stopping power of the proton is lower than that of the $\langle 100 \rangle$ and $\langle 111 \rangle$ channels; this trend is mainly attributed to the discrepancy in the channeling electronic density. In addition, our research gives evidence that the threshold velocity $v_{th} = 0.1294$ a.u. is closely related to the indirect band gap. That result suggests that only the valence band's electrons across the band gap can contribute to the electronic energy dissipation; therefore, we discuss that the defect state induced in the gap by the passing ion serves like an elevator ferrying the valence-band electrons across the indirect band gap. Last, we investigate the charge accumulation and depletion as an energy-loss model by intuitive charge-density difference. Furthermore, the intensity of the chemical bond between the projectile and the host atoms around the channel is indirectly investigated and analyzed by obtaining the amplitude of the electron localization function. The shortening and elongation of the chemical bond are deemed a mechanism of the electronic energy loss in the process of the ion-solid interaction, which can contribute to the electronic stopping power. These results supply reference data for the application of the excellent material TiN in ion-beam irradiation.

I. INTRODUCTION

As we all know, when a material is exposed to an irradiation environment, radiation over a certain level will lead to an irreversible deterioration of its performance. In this process, it is vital to understand how radiation damage in a material is caused and evolves over time [1,2]. When an energetic ion passes through the material, it deposits energy in the material due to the interaction with the atoms of the material. Such an effect is of great interest in a wide range of research fields, such as nanotechnology (e.g., material modification) [2,3], health physics (e.g., ion-beam therapy for cancer) [4], space exploration (e.g., spacecraft) [5], and nuclear safety (e.g., the irradiance resistance of materials in nuclear reactors) [6], among others. The essence of the irradiation damage is the ionic energy deposition caused by the interaction between energetic charged ions and target materials. Therefore, an analysis of the electronic stopping power of ions is a fundamental problem of studying the irradiation-damage mechanism and anti-irradiation properties of materials. The energy-transfer rates in the collisions of an ion with the target nuclei and electrons are defined as the nuclear stopping power S_n and the electronic stopping power S_e, respectively.

As a key physical quantity, S_e is the electronic energy-loss rate per unit path length, i.e., $S = dE/dx$. In the case of a slow ion through a material, i.e., ionic velocity $v \leqslant v_F$ (v_F is the Fermi velocity), S_e exhibits velocity proportionality due to the projectile ion interacting only with weakly bound electrons in the conduction or valence band of the target material. Because the thickness and size of electronic devices are decreasing at present, the energy loss of low-energy ions is also of great significance for ion implantation of nanoscale materials. Recently, special-interest studies have been carried out in the velocity range $v \leqslant 1.0$ a.u. (atomic units with $|e| = m = \hbar = 1$ are used hereafter); for light ions, the time-dependent density-functional theory (TDDFT) [7–9] is extensively used to calculate S_e for a homogeneous electron gas (HEG) representing the intended material, and the calculated results are in good agreement with the experimental values [10–22]. Therefore, this method has the ability to predict S_e of the low-energy light ion in the target material.

In this velocity regime, besides the influence of electronic excitations, charge transfer, and electronic structure on S_e, the influence of the chemical process (e.g., the breaking, forming, or change of chemical bonds in the time-evolution process) during the collision should be taken into account. The intuitive

___
*Corresponding author: fszhang@bnu.edu.cn

concept of a chemical bond is very concise and straightforward: an electron pair shared between neighboring atoms that provides the necessary attraction for binding the molecule. However, it is very difficult to define accurately what a bond is or even to imagine it. In addition, the channeling phenomenon plays a crucial role in the irradiation damage of crystalline materials, which is applied in the implantation technology related to device fabrication [23].

In this work, we report S_e of a slow proton ($v \leqslant 1.0$ a.u.) in TiN through the TDDFT calculation. Our results are quantitatively compared with existing experimental results, and there is good consistency between them. Moreover, S_e in different channels are investigated and analyzed, where S_e presents the direction dependence related to the discrepancy in the channeling electronic density and the stopping force. The channeling electronic density and the stopping force exhibit cyclic oscillations, which suggest a periodic arrangement of atoms in the crystalline TiN. For S_e of the wide-band-gap TiN, the threshold velocity indicates that the projectile ion in the band structure of the bulk Ge serves as an elevator and ferries the valence band's electrons across the band gap; this indirect electronic excitation possibly acts as an additional energy dissipation channel. Meanwhile, the existence of a relationship between the threshold velocity and the band gap of the medium is confirmed. Furthermore, the charge accumulation and depletion process is intuitively investigated with the aid of the charge-density difference, and the effect of the shortening and elongation of the chemical bond on S_e is quantitatively explored. The results indicate that the charge accumulation and depletion play a crucial role in electronic energy loss in addition to the electron-hole excitation.

Section II of this paper introduces the employed calculation method and the constructed crystal model. The results and discussion are presented in detail in Sec. III, and we give numerical results established with the TDDFT calculations compared with the experimental data. Section IV outlines and summarizes the main conclusions and results.

II. CALCULATION METHODS AND CRYSTAL STRUCTURES

The projectile ion passing through the crystal is conducted under channeling conditions during the simulation process. The dynamic-collision calculation is performed by employing the Ehrenfest dynamics time-dependent density-functional theory (ED-TDDFT) [24–30] based on the OCTOPUS *ab initio* code [31–33].

Therefore, the force of the nuclear motion is estimated by Ehrenfest classical dynamics theory, while the evolution of the electronic density and the system energy with time are described by the time-dependent Kohn-Sham (KS) equations [34,35] as follow:

$$i\dot{\varphi}_i(\vec{r}, t) = \left(-\frac{1}{2}\nabla^2 + V_{KS}[n](\vec{r}, t)\right)\varphi_i(\vec{r}, t). \tag{1}$$

Here the electronic density n at time t is obtained by summing the individual electron probabilities, i.e., $n(\vec{r}, t) = \sum_{i=1}^{N} |\varphi_i(\vec{r}, t)|^2$, and N denotes the number of electrons in the system. $\vec{r}$ and t are the spatial and time coordinates, respectively.

Therefore, the KS effective potential $V_{KS}[n](\vec{r}, t)$ is written as

$$V_{KS}[n](\vec{r}, t) = V_{ne}(R(t), \vec{r}) + \int d^3r' \frac{n(\vec{r}', t)}{|\vec{r} - \vec{r}'|}$$
$$+ V_{XC}[n](\vec{r}, t), \tag{2}$$

where $V_{ne}(R(t), \vec{r})$ is the time-dependent interaction potential between electrons and nuclei [at ionic positions $R(t)$]. The second term denotes the Hartree potential including the classical electron-electron interactions. The last term, $V_{XC}[n](\vec{r}, t)$, represents the time-dependent exchange-correlation (TDXC) potential. In the present model, the adiabatic local-density approximation with Perdew-Wang parametrization [36] is employed for the TDXC potential. We use the norm-conserving Troullier-Martins pseudopotential [37] to describe the interaction potential V_{ne} between electrons and nuclei.

The target material we establish is the $2 \times 2 \times 2$ conventional supercell comprising 32 Ti atoms and 32 N atoms with the F-43M (No. 216) symmetrical space group. The chosen lattice parameter is 4.6024 Å, which is consistent with the experimentally reported value in Ref. [38]. First, the supercell is placed in the center of a parallelepiped simulation box. In this simulation unit, the KS orbitals, electronic density, and potentials are discretized on a set of grid points with uniform spacing of 0.16 Å along the XYZ spatial coordinates. The proton as a projectile is placed outside the simulation box, and we obtain the unperturbed electronic density distribution that acts as the initial structure. Shortly after, the proton is initialized with a velocity derived from the specified incident energy and moves rectilinearly through the target TiN along different channels (i.e., in this case, along the negative direction of the z axis). We use a time step of 1 as for the proton propagation in order to ensure stable calculation results.

III. RESULTS AND DISCUSSION

A. The channeling effect

In Fig. 1, we present the theoretical results for S_e of the proton in TiN, together with the experimental result of Sortica *et al.* [39]. The predicted data from SRIM-2013 [41,42] as the reference values are also shown in Fig. 1 and are based on fitting to a large number of experimental data and extrapolation from Bragg's rule. S_e of the proton along the $\langle 100 \rangle$, $\langle 110 \rangle$, and $\langle 111 \rangle$ channels are investigated using the ED-TDDFT simulation. For the channel-center directions, the calculated values are below the experimental data and SRIM curve; these results are partly expected for various reasons. First of all, the proton travels through the center of the channels (i.e., having low electron density). Second, the experimental data and SRIM values are obtained by averaging a large number of random trajectories. Third, the proton does not sufficiently excite the electrons around the host atoms under the channel-center conditions.

For this reason, we investigate three parallel off-center channeling trajectories with different impact parameters (i.e., a different closest distance to any of the nitrogen atoms around the projectile trajectory) in the $\langle 100 \rangle$ direction, as shown in the
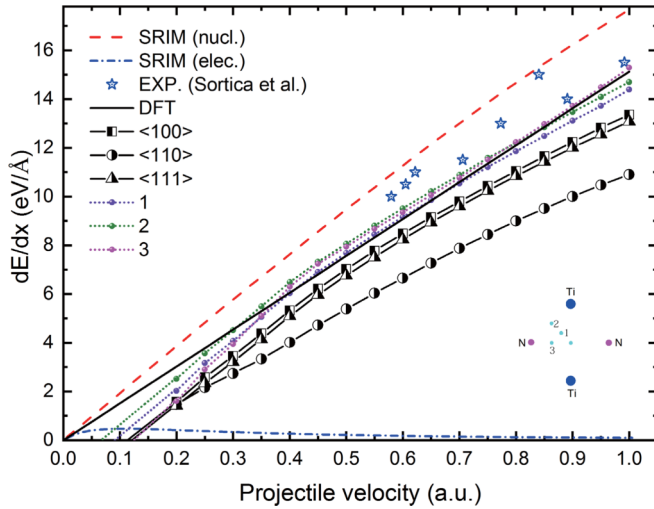
FIG. 1. Electronic stopping power of the proton in TiN vs the projectile velocity v for the channel-center trajectories (black lines) and for the off-center channeling trajectories (dotted lines). The inset presents a sectional view of the $\langle 100 \rangle$ channel including the sites of center and off-center channeling trajectories. The dashed lines refer to the SRIM-2013 predictions. The blue stars show the experimental data from Sortica *et al.* [39]; the solid black line is the predication using the DFT method (data taken from [40]). The curves of S_e are extrapolated to the velocity range $v < 0.2$ a.u. by fitting the values from 0.2 to 0.45 a.u.

inset in Fig. 1; the corresponding S_e is presented. The channel center has the most significant impact parameter; the trajectories close to the edge of the channel center have the lowest impact parameter. We find that S_e rises as the impact parameter decreases, which indicates that the impact parameter plays a substantial role in the process. As expected, the smaller impact parameter increases the value of S_e, which brings S_e into better agreement with the existing experimental data [39] and prediction based on the density-functional-theory (DFT) model [40].

As shown in Fig. 1, a notable phenomenon is that S_e exhibits direction dependence in this velocity regime. The S_e results for the $\langle 100 \rangle$ and $\langle 111 \rangle$ channels are basically the same and are higher than S_e of the $\langle 110 \rangle$ channel. This trend can be interpreted as the difference in the electronic density in the $\langle 100 \rangle$, $\langle 110 \rangle$, and $\langle 111 \rangle$ channels. For this reason, we investigate the channeling electronic density of the ground state; the results are shown in Fig. 2. The way to compute this quantity is to integrate the electronic density within a small cylinder with radius $r = 0.32$ Å along the center of the channel; the total number of electrons for each step is obtained in turn and is divided by the volume of the corresponding small cylinder step by step. We find that the channeling electronic densities of the $\langle 100 \rangle$ and $\langle 111 \rangle$ channels are more prominent than that of the $\langle 110 \rangle$ channel, so the electron distribution of the $\langle 110 \rangle$ channel is the most dilute and belongs to the electron-poor channel. Furthermore, the amplitude of the other two channels is significantly larger than that of the $\langle 110 \rangle$ channel; the cyclic fluctuation of the channeling electronic density demonstrates the periodic arrangement of atoms in the target material. These results indicate that the repeated charge exchange in
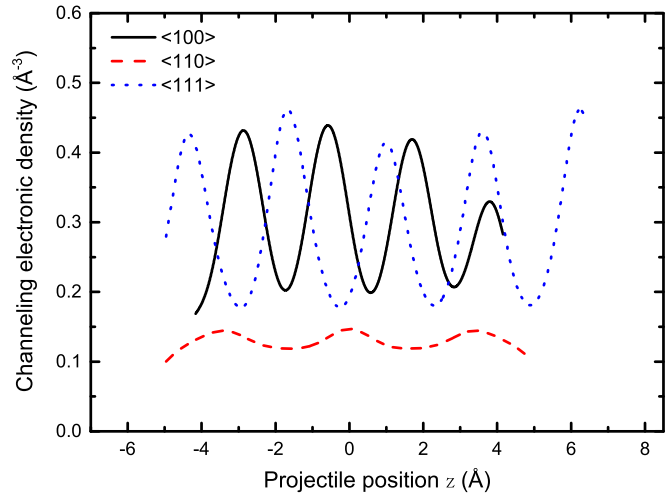

FIG. 2. The electronic density of the $\langle 100 \rangle$ (black solid line), $\langle 110 \rangle$ (red dashed line), and $\langle 111 \rangle$ (blue dotted line) channels.

the crystal will happen and contribute to S_e. Along with a low electronic concentration and small fluctuation channel, e.g., the $\langle 110 \rangle$ channel, the electronic energy loss is lower due to the weak excitations of the electron-hole pairs, which leads to a small S_e. Obviously, the behaviors of the channeling electronic density coincide with the channeling S_e trend in Fig. 1. Therefore, the channeling effect of S_e is strongly linked to the channeling electronic density of the ground state, which is similar to the conclusions reported in the Ref. [43]. In addition, the channeling effect also depends on other parameters (e.g., including the critical angle, the distance of the closest approach, and the channeling-dip depth), which is worth studying more in depth in the future.

In addition, the value of the ionic stopping force is tracked during the simulations; we present here the stopping force acting on the 0.6-a.u. proton in different channels (Fig. 3). We find that the stopping forces oscillate as the proton moves along the different channels, where the projectile ion is viewed
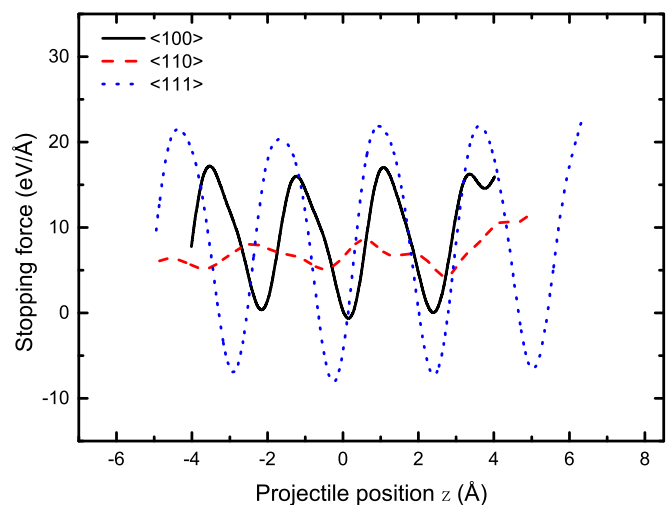

FIG. 3. The stopping force of the proton with a velocity of 0.6 a.u. traveling through the target TiN along the $\langle 100 \rangle$ (black solid line), $\langle 110 \rangle$ (red dashed line), and $\langle 111 \rangle$ (blue dotted line) channels.
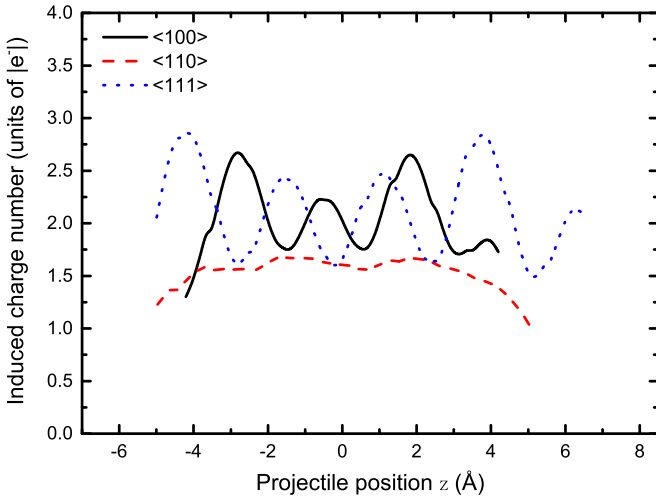
FIG. 4. The total number of induced charges around the proton for the proton with a velocity of 0.6 a.u. traveling through the target TiN along the $\langle 100 \rangle$ (black solid line), $\langle 110 \rangle$ (red dashed line), and $\langle 111 \rangle$ (blue dotted line) channels.
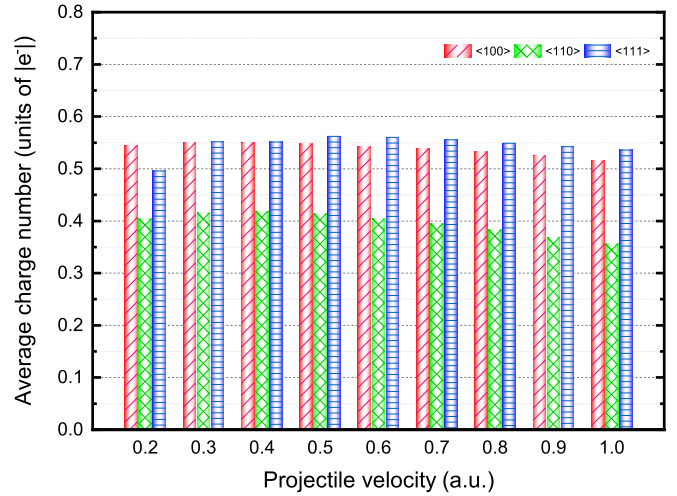

FIG. 5. The average number of induced charges around the proton for the proton traveling through the target TiN along the $\langle 100 \rangle$ (red diagonal-line bars), $\langle 110 \rangle$ (green crossed-line bars), and $\langle 111 \rangle$ (blue transverse-line bars) channels at different velocities. The mean numbers for the proton with different velocities in the $\langle 100 \rangle$, $\langle 110 \rangle$, and $\langle 111 \rangle$ channels are 0.539, 0.396, and 0.545 units of $|e^-|$, respectively.

as a periodic perturbation to the crystalline TiN. The magnitude of force indicates the Coulomb interaction intensity between the proton and the host atoms around the channel. As one can see, the amplitude of the stopping force in the $\langle 100 \rangle$ and $\langle 111 \rangle$ channels is much greater than that of the stopping force in the $\langle 110 \rangle$ channel; this trend is similar to that of the channeling electronic density. These features indirectly imply that the Coulomb excitation can contribute to the energy loss. Additionally, we find that the stopping force and the electronic density of the corresponding channel have a similar fluctuation, which potentially implies a proportional relationship between them.

When the energetic projectile passes through the crystalline medium, it is able to induce and excite the channeled electrons and is subsequently wrapped by these induced electrons, forming a layer of an electron cloud. The process of electronic transfer between the projectile ion and the host atoms is accompanied by excitation and ionization as well as electron-following behaviors, in which the electron shifts from the valence band of the host atom to the bound state of the ion or vice versa. This transition between the host atom of the medium and the projectile ion brings about energy dissipation of the projectile.

To investigate the effect of induced charge on the electronic energy loss, as shown in Fig. 4, we calculate the induced charge as a function of the projectile position for the proton in the $\langle 100 \rangle$, $\langle 110 \rangle$, and $\langle 111 \rangle$ channels. The number of charges induced by the projectile ion is extracted by quantitatively integrating the valence electronic density in the spherical volume with a radius of $r = 1.12$ Å around the projectile ion and subtracting the number of charges in the ground state within the corresponding spherical volume. The total number of charges induced in each step is sequentially obtained; the induced charges in the entire trajectory are thus obtained step by step. A noticeable phenomenon is that the induced charges around the intruding ion are found to keep oscillating up and down when it permeates along different channel midaxes of the crystalline TiN, where the oscillation indicates the charge

follow and loss (i.e., the induced charge). A fluctuation trend similar to the channeling electronic density is found in the channeling-induced charge, which indicates that the proton moving along the high channeling electronic density is conducive to promoting the projectile ion stripping electrons from the channeling host atoms.

Furthermore, the periodic oscillation of the induced charge with the trajectory implies that the lattice layer is strictly periodic in time and space. Compared with the mild behavior of the proton in the $\langle 110 \rangle$ channel, the perturbation charge process for the proton in the other two channels is very active; an evident phenomenon is that the drastic charge follow-and-release process alternatively takes place, which is deemed a channel of the electronic energy dissipation. Moreover, for a proton with different velocities along the whole path, Fig. 5 shows that there is a dramatic difference in the average induced charge number of the $\langle 110 \rangle$ channel compared with that of the $\langle 100 \rangle$ and $\langle 111 \rangle$ channels. Therefore, the $\langle 100 \rangle$ and $\langle 111 \rangle$ channels present large S_e values; the mean values at different velocities in the corresponding channels are 0.539 and 0.545 in units of $|e^-|$, respectively. This phenomenon demonstrates that the charge transfer results in the electronic energy loss.

B. The threshold effect of S_e

As shown in Fig. 1, for the proton, an apparent threshold velocity of $v_{th} = 0.1294$ a.u. is found by extrapolating the linear S_e toward lower velocities. In Refs. [44,45], the authors reported a threshold velocity below which a slow-velocity proton traveling through the insulator LiF cannot exchange enough energy to excite the electrons of the medium to cross the band gap. Below this threshold velocity, S_e would be strictly suppressed to zero (i.e., vanishing electronic stopping power). To estimate the relation of the threshold velocity and
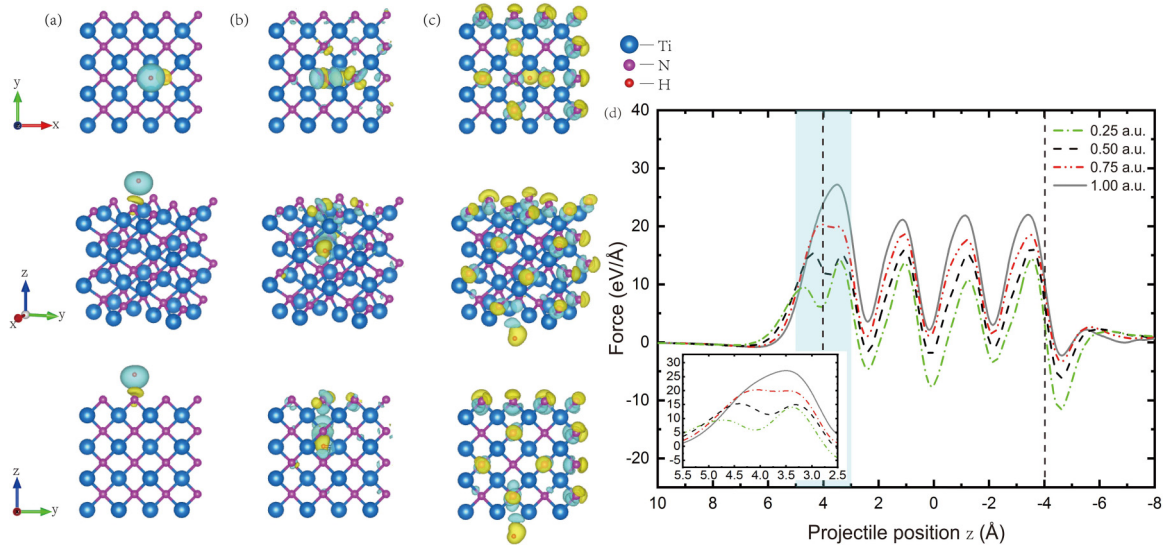
FIG. 6. Charge-density difference for the 0.3-a.u. proton in the TiN bulk (along the ⟨100⟩ channel) with an isosurface value of 0.037 $e/\mathring{A}^3$. (a) is the charge-density difference of the primary stage, and (b) and (c) are the charge-density differences of the excited state for $t = 1.43$ and 2.42 fs. Yellow and light blue depict charge accumulation and depletion around the proton, respectively. The first row shows the top view, the second row shows the oblique view, and the third row shows the view along the x axis. (d) presents the force acting on the proton coordinate for four velocities: 0.25 a.u. (gray solid line), 0.50 a.u. (red dash-double-dotted line), 0.75 a.u. (black dashed line), and 1.00 a.u. (green dash-dotted line). The vertical dashed lines represent the thickness of the crystalline film.

the band gap, we obtain the threshold value according to the method described in the literature [46]. A projectile ion passing through the crystalline medium along the channel is able to induce an oscillation of time-varying potential at the passing frequency of atoms, i.e., $f = v/\lambda$, where v and λ are the projectile velocity and the equivalent lattice-point distance, respectively. In this study, the equivalent lattice-point distance $\lambda = 3.2544$ Å, which is taken from the distance between the nearest N-N atoms (or the nearest Ti-Ti atoms). Therefore, with the aid of a band gap Δ equal to hf (where h denotes Plank's constant), we obtain the following threshold-velocity expression:

$$v_{\text{th}} = \frac{\lambda \Delta}{h}. \tag{3}$$

The result reported in Ref. [47] shows TiN thin films with a wide band gap $\Delta = 3.4$ eV; based on Eq. (3), the threshold velocity across the band gap is calculated to be 0.1222 a.u. This threshold value is in good agreement with our result ($v_{\text{th}} = 0.1294$ a.u. in Fig. 1) obtained with the TDDFT simulation. A threshold velocity of $v_{\text{th}} = 0.1294$ a.u. is obtained by averaging four threshold values for different parallel channels, as shown in Fig. 1, where four threshold velocities are obtained from extrapolating curves down by a linear fit.

That is to say, to carry the electrons from the valence band to the conduction band across the gap, this ferrying process requires the minimum energy, so the kinetic energy of the projectile is able to promote the transfer of electrons. Horsfield *et al.* [48] and Lim *et al.* [46] pointed out that an energy-gap state induced by the tunneling ion serves as an elevator and ferries the electrons of the valence band across the band gap (as shown in the schematic drawing in Fig. 3 of Ref. [48]). The specific process is that the energy of this energy gap state fluctuates within the band gap when the projectile ion passes

through the crystalline medium. When the state is close to the valence band, it can collect electrons from the filled state. In a like manner, it can deposit electrons into the empty conduction states when the state is close to the conduction band.

C. The electronic energy-loss mechanism

1. The energy-loss channel: Charge accumulation and depletion

To further estimate the effect of charge excitation and transfer on the energy loss, we investigate the charge-density difference based on Eq. (4) to describe and analyze the distinction between the ground state and excited state in the TiN film induced by the proton. The specific method to map the charge-density difference is by subtracting the charge-density distribution of the ground-state TiN and isolated proton from the charge-density distribution of the TiN perturbed proton system as follows:

$$\Delta \rho = \rho_{\text{TiN/H}^+} - \rho_{\text{TiN}} - \rho_{\text{H}^+}, \tag{4}$$

where $\rho_{\text{TiN/H}^+}$, ρ_{TiN}, and ρ_{H^+} represent the electronic densities of a proton perturbing the TiN system, the pristine unperturbed TiN system, and isolated proton, respectively.

Figure 6 exhibits the charge accumulation (in yellow) and depletion (in light blue) between the projectile and the crystalline TiN film. Figure 6(a) shows the charge-density difference of the perturbed system at the primary stage. We find only a low proportion of the charge accumulation and depletion phenomenon. Figures 6(b) and 6(c) show the striking charge-density difference at $t = 1.43$ and 2.42 fs when a proton with a velocity of 0.3 a.u. enters the target TiN film along the ⟨100⟩ channel, respectively. Figure 6(b) shows the time when the applied invading projectile perturbation shows maximum amplitude behavior, while Fig. 6(c) illustrates the time when the projectile perturbation ends.

Substantial charge-accumulation behavior around the projectile indicates that the proton interacts robustly with the crystalline TiN.

For this reason, the force acting on the proton coordinate is evaluated and shown in Fig. 6(d); the energy loss of collisions is mainly attributed to the excitation of the valence electrons through Coulomb scattering. We can see that the acting force is sensitive to the proton velocity. In the force range from 3 to 5 Å (light-blue area) the multiple fluctuations of the interaction demonstrate the active charge accumulation and depletion phenomenon. However, only a small fraction of the charge transfer occurs [in the primary stage; Fig. 6(a)], which implies weak interaction between the proton and TiN [the light-blue region shown in Fig. 6(d)]. The resonant excitation is considered a path for energy loss [49]; the driving-force frequency of the projectile ion fails to reach the inherent frequency of the electrons in the target lattice when the projectile gets close to and enters the target material. The fluctuation of the interaction force does not reach the same frequency as the periodic crystalline target until the projectile ion reaches the position of $z = 3.2$ Å. After that, the electrons around the host atom are periodically induced to undergo a resonant excitation process, leading to energy loss or dissipation behavior. As a result, the electronic excitation can give rise to the charge accumulation and depletion, which are a contributing factor to the energy loss during the collision process, which provides insight into the energy-loss mechanism.

In addition, we find that the force acts continuously after the penetration ends when the projectile velocity is 0.25 a.u. The continuing existence of the interaction force indicates that there is still charge accumulation and depletion behavior. Therefore, there is delayed energy-loss behavior for the slow projectile tunneling the target TiN.

2. The energy-loss channel: Chemical bonds

When the projectile passes through the medium material, the electronic energy loss in this process is ascribed to the ionization, the electron-hole pair excitation, and the charge exchange; in addition, the shortening and elongation of the chemical bonds between the projectile ion and the host atoms play a vital role in the process of energy loss. The intuitive definition of the chemical bond is straightforward and elegant; that is, the electron pair shared (localization attractor) between neighboring atoms provides the necessary attraction to bind the molecule. Nevertheless, it is difficult to quantitatively describe a specific bond or to visualize it.

The time-dependent electron localization function (ELF) [50–52] is regarded as a function crafted to demonstrate the bond change (including the formation, breaking, and modulation of the chemical bonds) in the electronic system. $D_\sigma(\vec{r}, t)$ is defined as the probability of finding a second like-spin electron around the reference electron at position $\vec{r}$ and time t; a smaller probability indicates that the reference electron is more highly localized. For an electron system with a many-body wave function, $D_\sigma(\vec{r}, t)$ is expressed as

$$D_\sigma(\vec{r}, t) = \tau_\sigma(\vec{r}, t) - \frac{1}{4}\frac{[\boldsymbol{\nabla}\rho_\sigma(\vec{r}, t)]^2}{\rho_\sigma(\vec{r}, t)} - \frac{j_\sigma^2(\vec{r}, t)}{\rho_\sigma(\vec{r}, t)}, \quad (5)$$

where σ and ρ_σ represent the spin and spin density, respectively. j_σ is the absolute value of the current density, and

$$\tau_\sigma(\vec{r}, t) = \sum_{i=1}^{N_\sigma} |\boldsymbol{\nabla}\varphi_{i\sigma}(\vec{r}, t)|^2. \quad (6)$$

The parameter τ_σ denotes the kinetic-energy density of a system of N_σ electrons, which is described by the single-particle orbitals $\varphi_{i\sigma}$ obtained from TDDFT. The time-dependent ELF is written as

$$f_{\mathrm{ELF}}(\vec{r}, t) = \frac{1}{1 + \left[D_\sigma(\vec{r}, t)/D_\sigma^0(\vec{r}, t)\right]^2}; \quad (7)$$

therefore, the definition

$$D_\sigma^0(\vec{r}, t) = \tau_\sigma^{\mathrm{HEG}}(\rho_\sigma(\vec{r}, t)), \quad (8)$$

where

$$\tau_\sigma^{\mathrm{HEG}}(\rho_\sigma) = \tfrac{3}{5}(6\pi^2)^{2/3}\rho_\sigma^{5/3} \quad (9)$$

is the kinetic-energy density of a HEG with density ρ_σ. In this case, the quantity f_{ELF} is dimensionless; the values range from 0 to 1, with a value of 1 (i.e., $D_\sigma = 0$) indicating perfect localization and a value of 0.5 denoting HEG-like pair probability [52].

In order to intuitively present the evolution of ELF over time, Fig. 7 depicts the local electronic density at different times for the 0.6-a.u. proton in TiN along the ⟨100⟩ channel. Before the simulation, the crystalline TiN is in the ground state [see Fig. 7(a)]. At $t = 0.42$ fs, the electronic system begins to get perturbed and excited by the proton. With the increase of the penetrating depth, a torus between the proton and the host atom around the channel is visually observed, and we also find a typical hydrogen-nitrogen single bond [Figs. 7(c) and 7(d)]. At $t = 1.05$ fs, the chemical bond is broken, but the shared packet between hydrogen and nitrogen is still present [Fig. 7(e)]. Finally, at $t = 1.16$ fs, the proton carries part of the excited electrons and leaves the system in a fairly localized packet [Fig. 7(f)].

The above phenomena clearly demonstrate that the major electronic excitation is substantially contributed by the projectile ion, in which the excited region is located around the ion. The disturbance in the charge density arises directly from the Coulomb interaction between the proton and the host atoms; another key contributing factor is associated with the stretched H-N covalent bond.

In the range of low energies, the chemical bond is deemed to be a mechanism that affects electronic energy loss [53–55], but there is a lack of quantitative analysis. Therefore, we indirectly investigate the shortening and elongation of the chemical bonds during the collisions by analyzing the amplitude of the ELF in Fig. 8. The higher ELF around the proton indicates a more stable chemical bond.

In Fig. 8, we find that the ELF fluctuates periodically with the penetrating depth, which once again implies a periodic arrangement of the atoms in the medium TiN. The peak and valley of the ELF represent the shortening and elongation of the chemical bond, respectively. In addition, it should be noted that the amplitude of the ELF in the N layers is larger than the amplitude of the ELF in the Ti layers, which indicates that the
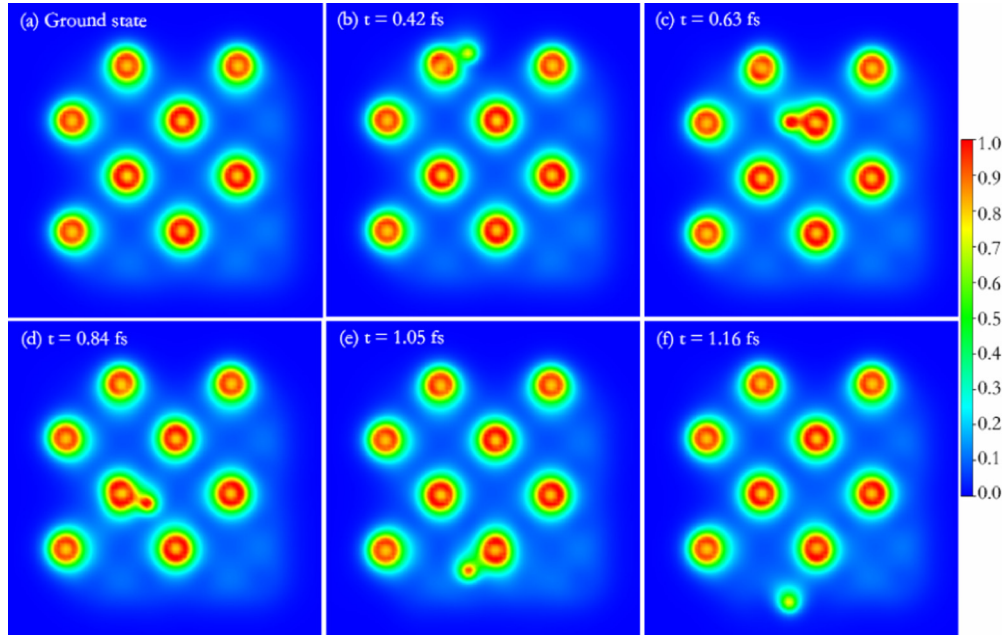
FIG. 7. Snapshots of the electronic density distribution for (a) the ground state without the projectile and (b)–(f) the state perturbed by the projectile with a velocity of 0.6 a.u. Note that the density distribution is plotted in the $y = y_{ion}$ (y_{ion}, i.e., the y coordinate value of the projectile ion) scattering plane.

H-N covalent bond is more stable than the H-Ti bond. This result is consistent with the trend shown in Fig. 7; that is, a more stable chemical bond is formed when the proton is close to the nitrogen atoms around the channel.

Furthermore, as shown in Fig. 8, the slow projectile with a higher ELF implies more stable chemical bonds between the proton and host atoms; thus, the kinetic energy of the proton dissipates, breaking the chemical bond. The amplitude of ELF in the whole path decreases with the increase of the projectile velocity. This trend demonstrates that, as the velocity of the projectile increases, the intensity of the chemical bonds be-
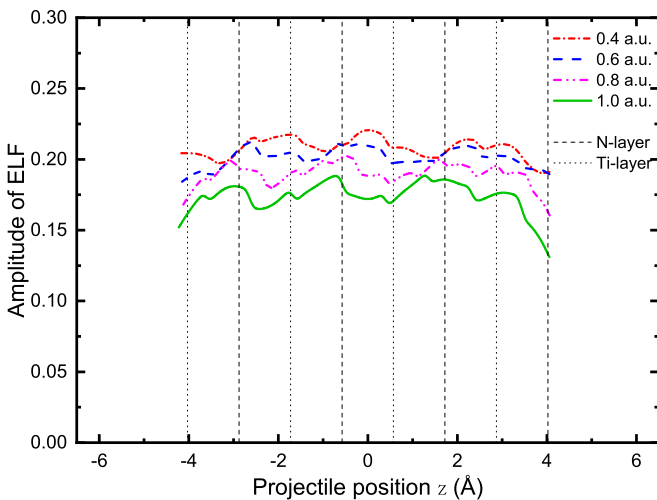
tween the proton and the host atoms around the channel is weakened. However, we note, for the projectiles with 0.8- and 1.0-a.u. velocity, that the ELF results present more intensive fluctuations, which indicates more active bond disruption and recombination. Since the chemical bond formation is only the dynamic of excited electrons, the projectile with the higher velocity results in frequent perturbed electrons. Therefore, in the case of high projectile velocity, more kinetic energy of the projectile is used to break the chemical bond. In addition, by analyzing the ELF for the channel center and off-center channel, we find that the chemical bond of the projectile through off-center channel shows a much more remarkable change, thus leading to more energy dissipation. These trends are in accordance with the trend of S_e shown in Fig. 1, implying that the shortening and elongation of the chemical bond are a path of electronic energy loss.

IV. CONCLUSIONS

In this study, the channeling effect of S_e for the slow proton in the medium TiN along different channels was investigated by analyzing the channeling electronic density and the stopping force, and we found that the trends of these two quantities coincide with that of S_e (i.e., the values of the ⟨100⟩ and ⟨111⟩ channels are more prominent than that of the ⟨110⟩ channel). Additionally, there is a proportional relationship between the channeling electronic density and the stopping force; the results (from the electronic density evolved over time along the projectile's entire track) once again demonstrate the quantitative relationship between the stopping force and the density as proposed by Lindhard and Winther [56]. The most apparent finding to emerge from this study is that, under the parallel off-center channel conditions, our calculated results are in good agreement with the experimental data.

FIG. 8. The average ELF in the spherical volume with a radius of 1.12 Å around the proton of different velocities along the ⟨100⟩ channel. The vertical dashed lines represent the N layers, and the dotted lines represent the Ti layers.

In addition, in the case of a proton passing through crystalline TiN, we found a threshold velocity of 0.1294 a.u. by extrapolating the linear S_e toward lower velocities, which is in very good agreement with the calculated threshold based on the band gap. A consistent comparison between the threshold obtained from the band gap and the reported values demonstrates that only the valence band's electrons across the band gap can cause the electronic energy loss in the low-energy region. When the projectile ion moves through the film medium, in the electronic band gap, the local electronic defect state induced by the passing ion serves as an elevator carrying the electrons in the valence band across the indirect band gap.

Furthermore, the present study laid out a detailed discussion of the electronic energy-loss mechanism. On the one hand, the charge accumulation and depletion process was recognized as a pathway of electronic energy loss by intuitively investigating the charge-density difference. On the other hand, with a quantitative estimation of the amplitude of the ELF, the results indicated that the chemical bonds between the projectile and the host atoms around the channel have a significant effect on S_e. The shortening and elongation of the chemical bond were quantitatively demonstrated to be a mechanism of the electronic energy dissipation. These results should help us to assess the impact of the chemical bond on S_e, i.e., to account for the trend of S_e as a function of the projectile velocity. More studies are needed to further investigate the role of the chemical bond in the electronic energy loss in theory and experiment.

[1] J. Koutský and J. Kocik, *Radiation Damage of Structural Materials*, Materials Science Monographs, Vol. 79 (Elsevier, Amsterdam, 1994).

[2] *Ion Beam Modification of Solids*, Springer Series in Surface Sciences, Vol. 61, edited by W. Wesch and E. Wendler (Springer, New York, 2016).

[3] S. Kim, S. Lee, and J. Hong, ACS Nano **8**, 4698 (2014).

[4] A. V. Solov'yov, E. Surdutovich, E. Scifoni, I. Mishustin, and W. Greiner, Phys. Rev. E **79**, 011909 (2009).

[5] O. Ilic, C. M. Went, and H. A. Atwater, Nano Lett. **18**, 5583 (2018).

[6] F. Komarov, A. Komarov, V. V. Pilko, and V. Pilko, J. Eng. Phys. Thermophys. **86**, 1481 (2013).

[7] E. Runge and E. K. U. Gross, Phys. Rev. Lett. **52**, 997 (1984).

[8] *Fundamentals of Time-Dependent Density Functional Theory*, Lecture Notes in Physics, Vol. 837, edited by M. A. L. Marques, N. T. Maitra, F. M. S. Nogueira, E. K. U. Gross, and A. Rubio (Springer, Berlin, 2012).

[9] C. A. Ullrich, *Time-Dependent Density-Functional Theory: Concepts and Applications* (Oxford University Press, Oxford, 2011).

[10] A. A. Correa, J. Kohanoff, E. Artacho, D. Sánchez-Portal, and A. Caro, Phys. Rev. Lett. **108**, 213201 (2012).

[11] R. Hatcher, M. Beck, A. Tackett, and S. T. Pantelides, Phys. Rev. Lett. **100**, 103201 (2008).

[12] M. Quijada, A. G. Borisov, I. Nagy, R. Díez Muiño, and P. M. Echenique, Phys. Rev. A **75**, 042902 (2007).

[13] M. A. Zeb, J. Kohanoff, D. Sánchez-Portal, A. Arnau, J. I. Juaristi, and E. Artacho, Phys. Rev. Lett. **108**, 225504 (2012).

[14] L. N. Serkovic Loli, E. A. Sánchez, O. Grizzi, and N. R. Arista, Phys. Rev. A **81**, 022902 (2010).

[15] M. A. Zeb, J. Kohanoff, D. Sánchez-Portal, and E. Artacho, Nucl. Instrum. Methods Phys. Res., Sect. B **303**, 59 (2013).

[16] A. A. Correa, Comput. Phys. Commun. **150**, 291 (2018).

[17] J. Halliday and E. Artacho, Phys. Rev. B **100**, 104112 (2019).

[18] E. E. Quashie and A. A. Correa, Phys. Rev. B **98**, 235122 (2018).

[19] E. E. Quashie, B. C. Saha, and A. A. Correa, Phys. Rev. B **94**, 155403 (2016).

[20] V. U. Nazarov, J. M. Pitarke, Y. Takada, G. Vignale, and Y.-C. Chang, Phys. Rev. B **76**, 205103 (2007).

[21] G. d. M. Azevedo, P. Grande, and G. Schiwietz, Nucl. Instrum. Methods Phys. Res., Sect. B **164–165**, 203 (2000).

[22] E. E. Quashie, R. Ullah, X. Andrade, and A. A. Correa, Acta Mater. **196**, 576 (2020).

[23] *Ion Implantation: Basics to Device Fabrication*, edited by E. Rimini (Springer Science & Business Media, New York, 1994), Vol. 293.

[24] D. Marx and J. Hutter, *Ab Initio Molecular Dynamics: Basic Theory and Advanced Methods* (Cambridge University Press, Cambridge, 2009).

[25] J. le Page, D. Mason, and W. Foulkes, J. Phys.: Condens. Matter **20**, 125212 (2008).

[26] A. Caro, A. A. Correa, A. Tamm, G. D. Samolyuk, and G. M. Stocks, Phys. Rev. B **92**, 144309 (2015).

[27] X. Li, J. C. Tully, H. B. Schlegel, and M. J. Frisch, J. Chem. Phys. **123**, 084106 (2005).

[28] X. Andrade, A. Castro, D. Zueco, J. Alonso, P. Echenique, F. Falceto, and A. Rubio, J. Chem. Theory Comput. **5**, 728 (2009).

[29] A. P. Horsfield, D. Bowler, A. Fisher, T. N. Todorov, and M. Montgomery, J. Phys.: Condens. Matter **16**, 3609 (2004).

[30] C. Race, *The Modelling of Radiation Damage in Metals Using Ehrenfest Dynamics* (Springer, 2011).

[31] M. A. Marques, A. Castro, G. F. Bertsch, and A. Rubio, Comput. Phys. Commun. **151**, 60 (2003).

[32] X. Andrade, J. Alberdi-Rodriguez, D. A. Strubbe, M. J. Oliveira, F. Nogueira, A. Castro, J. Muguerza, A. Arruabarrena,

S. G. Louie, A. Aspuru-Guzik, A. Rubio, M. A. L. Marques, J. Phys.: Condens. Matter **24**, 233202 (2012).

[33] X. Andrade, D. Strubbe, U. De Giovannini, A. H. Larsen, M. J. Oliveira, J. Alberdi-Rodriguez, A. Varas, I. Theophilou, N. Helbig, M. J. Verstraete, S. Lorenzo, N. Fernando, A. Aspuru-Guzik, A. Castro, M. A. L. Marques, A. Rubio, Phys. Chem. Chem. Phys. **17**, 31371 (2015).

[34] A. Zangwill and P. Soven, Phys. Rev. A **21**, 1561 (1980).

[35] A. Schleife, E. W. Draeger, Y. Kanai, and A. A. Correa, J. Chem. Phys. **137**, 22A546 (2012).

[36] J. P. Perdew and Y. Wang, Phys. Rev. B **45**, 13244 (1992).

[37] N. Troullier and J. L. Martins, Phys. Rev. B **43**, 1993 (1991).

[38] K. Persson, Materials data on TiN (SG:216) by Materials Project, https://materialsproject.org/docs/calculations.

[39] M. A. Sortica, V. Paneta, B. Bruckner, S. Lohmann, T. Nyberg, P. Bauer, and D. Primetzhofer, Sci. Rep. **9**, 176 (2019).

[40] M. A. Sortica, V. Paneta, B. Bruckner, S. Lohmann, M. Hans, T. Nyberg, P. Bauer, and D. Primetzhofer, Phys. Rev. A **96**, 032703 (2017).

[41] J. Ziegler, J. Biersack, M. Ziegler, D. Marwick, and G. Cuomo, SRIM-2013, http://srim.org.

[42] J. F. Ziegler, J. P. Biersack, and U. Littmark, *The Stopping and Range of Ions in Solids* (Pergamon, New York, 1985), Vol. 1.

[43] S. Yu, B. Bahrim, B. Makarenko, and J. W. Rabalais, Surf. Sci. **614**, 12 (2013).

[44] J. M. Pruneda, D. Sánchez-Portal, A. Arnau, J. I. Juaristi, and E. Artacho, Phys. Rev. Lett. **99**, 235501 (2007).

[45] F. Mao, C. Zhang, J. Dai, and F.-S. Zhang, Phys. Rev. A **89**, 022707 (2014).

[46] A. Lim, W. M. C. Foulkes, A. P. Horsfield, D. R. Mason, A. Schleife, E. W. Draeger, and A. A. Correa, Phys. Rev. Lett. **116**, 043201 (2016).

[47] M. Solovan, V. Brus, E. Maistruk, and P. Maryanchuk, Inorg. Mater. **50**, 40 (2014).

[48] A. P. Horsfield, A. Lim, W. Foulkes, and A. A. Correa, Phys. Rev. B **93**, 245106 (2016).

[49] Y.-N. Wang and Z. L. Mišković, Phys. Rev. A **66**, 042904 (2002).

[50] T. Burnus, M. A. L. Marques, and E. K. U. Gross, Phys. Rev. A **71**, 010501 (2005).

[51] B. Silvi and A. Savin, Nature (London) **371**, 683 (1994).

[52] A. D. Becke and K. E. Edgecombe, J. Chem. Phys. **92**, 5397 (1990).

[53] S. Cruz, J. Soullard, and R. Cabrera-Trujillo, Nucl. Instrum. Methods Phys. Res., Sect. B **83**, 5 (1993).

[54] J. Soullard, S. Cruz, and R. Cabrera-Trujillo, Nucl. Instrum. Methods Phys. Res., Sect. B **80–81**, 20 (1993).

[55] S. Cruz and J. Soullard, Nucl. Instrum. Methods Phys. Res., Sect. B **61**, 433 (1991).

[56] J. Lindhard and A. Winther, Mat. Fys. Medd. K. Dan. Vidensk. Selsk. **34**, 1 (1964).